Characterization of Structural Inhomogeneities in Porous Media

Lynn F. Gladden and Michael P. Hollewand
Dept. of Chemical Engineering, University of Cambridge, Cambridge, CB2 3RA, UK

Paul Alexander
Dept. of Physics, University of Cambridge, Cavendish Lab., Cambridge, CB3 OHE, UK

Recent studies have demonstrated that spatial heterogeneities in voidage and pore size, over lengthscales of 0.1–1 mm, significantly affect the transport of liquids within a given porous medium. Nuclear magnetic resonance imaging is used to probe the structure of porous catalyst support pellets, and four image analysis techniques characterize the degree and nature of heterogeneities observed in the spin-lattice relaxation-time images of six pellets taken from the same batch. Power-spectrum, cluster-size, and percolation analysis reveal significant differences in spatial correlations and topological characteristics of the six images. The fractal dimension of all the images, however, is the same suggesting that this quantity characterizes the intrinsic heterogeneities associated with the particular batch of porous pellets studied in this work. The results suggest that structural models of such pellets should account for these macroscopic variations in pellet structure, as characterized here.

Introduction

Transport within porous pellets depends strongly on the internal structure of the pellet. Much work, both experimental and theoretical, has been done to understand how the tortuosity and hence effective diffusivity within the pore space are affected by the pore-size distribution, pore shape, and the connectivity of the pore network (see Sahimi et al., 1990, for a recent review). In particular, attention is now being given to investigating the applicability and limitations of different modeling techniques such as the effective medium approximation (Kirkpatrick, 1973, and references therein; Sotirchos and Burganos, 1988; Sahimi, 1988) and "first passage time" Monte Carlo (Reyes and Iglesia, 1991) approaches. Inherent in many of these studies is a need to represent adequately the characteristics of the pore space that determine the associated transport properties. For example, when considering networks of low connectivity (< 6), it has been demonstrated that the topology (i.e., random or regular) of the network significantly influences the percolation threshold and cluster distributions characterizing networks of a given network connectivity (Hollewand and Gladden, 1992a). The implications of this observation have been shown for the case of modeling diffusion and reaction processes in random pore networks (Hollewand and Gladden, 1992b). Thus, if an experimental determination of the connectivity of a pore structure shows that the connectivity lies in the low-connectivity regime, it is important to perform transport simulations on networks of topology appropriate to the real sample of interest. Further studies have addressed the representation of pore shape (Burganos and Payatakes, 1992) and realistic representations of the voidage in numerical simulations of mono- and bidisperse structures (Reyes and Iglesia, 1991; Hollewand and Gladden, 1992c). The general conclusion that follows directly from these studies is that an accurate representation of the pore-size distribution, macroscopic heterogeneities in voidage, and the extent of disorder of such regions play a crucial role in determining the transport characteristics of a porous solid.

Recently we have used nuclear magnetic resonance (NMR) imaging to image directly macroscopic heterogeneities in

Correspondence concerning this article should be addressed to L. F. Gladden.

voidage and pore size within porous catalyst pellets. In particular, we observed that the lengthscale of structural inhomogeneities (typically $0.1 \rightarrow 1$ mm), as revealed by spin-lattice relaxation time NMR images, is the same as the dimensions of the inhomogeneities observed in self-diffusion images recorded using a PGSE preconditioned spin-echo imaging sequence (Hollewand and Gladden, 1993). Further it was observed that nominally identical porous catalyst pellets drawn from the same batch show significantly different internal structure on the micron scale. However, in all cases, the correspondence in lengthscale between inhomogeneities in both structure and transport images remained. Our studies together with those of other workers (Oger et al., 1992) provide evidence that structural inhomogeneities play an important role in determining the macroscopic transport properties of the pellet. It is the aim of this work to use a combination of image analysis techniques to quantify the nature of the disorder in the structure of porous pellets such that the essential characteristics of the porous system of interest may then be transferred to a numerical or theoretical representation of that system.

The degree of inhomogeneity observed in a system depends to some extent on the spatial scale to which a particular measurement technique is sensitive. If, in addition, objective analysis techniques are not employed, then the subjective perception of the experimenter or observer can give a completely false impression of the "structure" present. In this article we consider four quantitative methods of analysis (power spectra, cluster-size distribution, fractal dimensionality, and percolation threshold) and apply these to characterize structural inhomogeneities within images of six porous catalyst support pellets drawn from the same batch. Each of these techniques provides complementary information. The power spectrum is a traditional method for quantifying structure on different spatial scales; however, interpretation of the power spectra in the current context proved difficult. Cluster-size analysis is a simple, objective method of quantifying the "degree of order" perceived by eye. Calculation of the fractal properties of the image quantifies the shapes of homogeneous clusters within the image, while percolation analysis provides us with information on the connectedness of these clusters. In the six images of porous catalyst pellets presented here, the fractal dimensionality of all images are remarkably similar. In contrast, the power spectrum and cluster-size analysis of each image are quite different, as is the visible appearance of the six relaxation-time images. The percolation threshold is shown to be particularly sensitive to large-scale correlations within the image.

The results presented in this article suggest that a model describing the structure and associated transport processes of a typical porous pellet drawn from a particular sample batch should be characterized by the same fractal dimensionality as that determined experimentally, if the true properties of the porous medium are to be predicted. It is perhaps only at a second stage of refinement of the model that the structural implications of the power-spectrum, cluster-size, and percolation analysis associated with a single pellet should be incorporated. At this stage of sophistication, the model would be addressing the structural and transport properties of this specific pellet. This article also demonstrates additional insights into the nature of the pore space given by NMR images, beyond those obtained from the one-dimensional pore-size distributions derived from mercury porosimetry or nitrogen adsorption analysis. However, it is noted that the nitrogen- and mercury-based techniques still provide much useful information concerning the absolute pore sizes within the material, albeit that such analyses remain complicated by effects such as pore shielding (Lowell and Shields, 1984).

In earlier studies we have used NMR imaging techniques to reveal structural variations on different lengthscales within porous catalyst support pellets (Hollewand and Gladden, 1993). The aim of this article is to show how image analysis techniques can be used to obtain an objective characterization of these structural variations that may then be used in numerical simulations of transport in these systems. The structure of this article is as follows. First, a brief outline is given of the principles of NMR imaging, and the assumptions used in obtaining information on the structure of porous media using this technique are also provided. Spin-lattice relaxation images of six porous catalyst support pellets drawn from the same batch are then presented and their acquisition conditions stated. The six images are then analyzed using four image analysis techniques: power-spectrum analysis, cluster analysis, fractal dimensionality, and percolation threshold. Application of these methods to images of porous media is not well-established, and in some cases it was necessary to develop specific algorithms for application in this study. For this reason a section introducing the theoretical background to each technique and its practical implementation is included. The interpretation of the results obtained from these analyses and the implications of using these data in numerical simulations of transport in porous media are then discussed. Although porous catalyst pellets are the subject of this study, it is emphasized that the image analysis techniques described in this work can be applied to the analysis of an image produced by any tomographic technique, of any porous medium.

NMR Theory

Applications of NMR imaging are now well-established in areas of interest to materials scientists and chemical engineers (Callaghan, 1991). In NMR imaging, a magnetic field gradient, $\boldsymbol{G}$, is applied to the sample in addition to the uniform polarizing field B_0. The resultant precession frequency of the nuclear spins, ω, then becomes a function of position, $\boldsymbol{r}$, and is given by $\omega(\boldsymbol{r}) = \gamma B_0 + \gamma \boldsymbol{G} \cdot \boldsymbol{r}$, where γ is the gyromagnetic ratio of the nucleus under study. It may be shown that the signal, dS, in an element of volume dV, at position vector $\boldsymbol{r}$ associated with a spin density $\rho_s(\boldsymbol{r})$, is given by (Callaghan, 1991):

$$dS(\boldsymbol{G},t) = \rho_s(\boldsymbol{r}) dV \exp[i(\gamma B_0 + \gamma \boldsymbol{G} \cdot \boldsymbol{r})t]. \qquad (1)$$

Thus the density of spins is observed as a function of real-space position $\boldsymbol{r}$ and, in principle, all the techniques of solid and liquid state NMR may be modified to give spatially resolved information.

Following perturbation of the nuclear spin system by a radio frequency (rf) pulse, the magnetization vector associated with the sample under study while placed in the static magnetic field B_0 is rotated away from its equilibrium alignment

with B_0, thereby giving rise to components of both transverse and longitudinal magnetization relative to the equilibrium vector M_0. The exponential recovery of the longitudinal component of the magnetization to its equilibrium value is known as spin-lattice relaxation and occurs via the transfer of excess energy from the spin population to its surroundings (commonly referred to as the "lattice"). The time constant of the relaxation process is therefore known as the spin-lattice (or longitudinal) relaxation time, T_1. In this study, images are obtained and analyzed in which each image pixel represents an estimate of the T_1 characteristic of that specific region of the material.

Interpretation of spin-lattice relaxation, T_1, images

In this section we discuss briefly the physical interpretation of T_1 images of porous materials. Our principal motivation for studying T_1 images is that the lengthscales of inhomogeneities in T_1 and self-diffusion images are similar for every porous catalyst support pellet we have studied (Hollewand and Gladden, 1993). Further, under certain conditions (to be discussed later), the spin-lattice relaxation time correlates with the surface-to-volume ratio characteristic of the pore space under study. We note that the analysis presented here and the discussion of structural heterogeneities depend only on the T_1 images representing a measurable property of the material and not on the detailed interpretation of T_1 in a porous solid; however, any further inferences that can be drawn regarding the pore structure from the interpretation of spin-lattice relaxation time are clearly of additional value.

The NMR spin-lattice relaxation behavior of a fluid confined within a pore is sensitive to both the pore geometry and size; in particular, the rate of spin-lattice relaxation is enhanced due to interactions at the solid-liquid interface (Woessner, 1962). The simplest physical model that can be employed to interpret T_1 data is the two-fraction, fast-exchange model (Brownstein and Tarr, 1977) which, assuming that diffusion of the fluid to the surface is much faster than the relaxation process, leads to an observed relaxation rate that can be related to the pore structure:

$$\frac{1}{T_1} = \frac{1}{T_{1B}} + \frac{\lambda S}{V}\frac{1}{T_{1S}}, \tag{2}$$

where T_{1B} is the relaxation time characteristic of the bulk fluid, T_{1S} is the relaxation time characteristic of a surface layer of thickness λ, and S/V ($= 2/r$ for cylindrical pores) is the surface-to-volume ratio of the pore. This simple model has been applied extensively, especially by Smith and coworkers (e.g., Munn and Smith, 1987), to determine pore-size distributions in porous samples. Considerable work has been done to improve this model (see, e.g., Wilkinson et al., 1991), which has led to a more exact result for the mean lifetime, τ, of the spin magnetization due to fluid-solid interactions:

$$\tau(\rho, \mathfrak{D}) = \frac{1}{d(d+2)}\frac{r^2}{\mathfrak{D}} + \frac{1}{d}\frac{r}{\rho} \tag{3}$$

for slab, cylindrical, or spherical pores ($d = 1,2,3$, respectively) of radius r; ρ characterizes the relaxation rate at the interface; and $\mathfrak{D}$ is the bulk diffusion coefficient. Under conditions of fast diffusion this expression reduces to a form that is consistent with the second term on the righthand side of Eq. 2 (taking $d = 2$ and $\rho = T_{1S}$); however, if the surface relaxation contribution is very fast, then the dependence on pore size will be quadratic and not linear. In general an unambiguous physical interpretation of T_1 data therefore requires knowledge of the relative rates of both spin-relaxation and diffusion within the pore space.

An additional problem of interpretation results from diffusion of the imbibed fluid (in this case, water) within the pore space over the timescale of the relaxation experiment (Mendelson, 1991). For typical timescales of 10^{-3} to 1 s appropriate to this experiment this gives an effective averaging of the T_1 measurement over spatial scales of 1 to 100 μm. This is in fact comparable to our spatial resolution of 40 μm; therefore, diffusional averaging occurs mainly within individual pixels of our image with some slight averaging between adjacent pixels. It is important to remember therefore that the values of T_1 for a given pixel represent an average over all the pores within the volume represented by the image pixel. Finally, variation in T_1 may in principle occur due to chemical inhomogeneities in the porous material, leading to varying relaxation rates at the liquid-solid interface. For our experiment, however, high purity silicas were used, and both spin-echo and gradient-reversal images of these pellets have been recorded and found to be almost identical. This result confirms that the contrast observed in the images reported here is *not* associated with variations in magnetic susceptibility within the sample. In conclusion, it is not possible to specify the precise relationship between measured T_1 and pore size; however, we do expect variations in the measured T_1's to reflect variations in the underlying structure of the pore space.

Experimental Studies

^{1}H NMR imaging experiments were performed using a Bruker Spectrospin MSL 200 NMR spectrometer with a static field strength of 4.7 T, yielding a proton resonance frequency of 200.13 MHz. Spin-lattice relaxation images were obtained using a spin-echo pulse sequence employing 90° selective and 180° nonselective pulses, the imaging sequence being preconditioned using a saturation-recovery pulse sequence; an echo time of 3.3 ms was used. The images consisted of 128 × 128 pixels and the read gradient strength was 56 G cm^{-1}, yielding an in-plane resolution of approximately 40 μm. A 90° Gaussian slice selective pulse truncated at 10 percent of maximum intensity was employed; the slice gradient strength and the image slice thickness were 10.6 G cm^{-1} and 0.45 mm, respectively. In order to obtain the signal-to-noise ratio for the determination of the T_1 map, between 60 and 120 scans were required, depending on the voidage of the pellet, which varied significantly from pellet to pellet. The T_1 images were obtained from eight to twelve T_1-weighted spin-echo images. The variable T_1 contrast was obtained by varying the repetition time (the time between each of the phase-encode steps in the imaging pulse sequence), TR, in the range $0.1T_1 < \mathrm{TR} < 3T_1$. The samples studied were high-purity silica spheres of approximately 2.2 mm diameter, characterized by a unimodal pore-size distribution centered at approximately 0.02 μm. A detailed characterization of these samples

is given in Hollewand and Gladden (1993). Each pellet was impregnated with deionized water (Hollewand and Gladden, 1993) and then placed in a sealed glass tube; in all the data sets presented, less than 5 percent of the initial moisture content was lost during the experiment. The experimental acquisition time varied between 6 and 14 hours.

To obtain a T_1 image, the signal intensity S from the same pixel, i, in each image is fitted to the expression describing the magnetization recovery appropriate to the saturation recovery experiment (Fukushima and Roeder, 1981):

$$S(i,\mathrm{VD}) = \rho_s(i)[1-\exp(-\mathrm{VD}/T_1(i))], \qquad (4)$$

where VD is the variable delay time in the saturation-recovery preconditioning pulse sequence, thereby obtaining a value of $T_1(i)$ and $\rho_s(i)$ for pixel i. By repeating this procedure for each pixel in the image, a complete image of relaxation time and spin density within the sample is produced. Only the spin-lattice relaxation time image for each sample is used in this article.

Images of the six catalyst pellets that we shall refer to as A1, A2, . . . , A6, are shown in Figure 1. It is apparent from the images that the pellets show very different inhomogeneities in their structure. In Figure 2 we show one (arbitrary) slice through each of the images to emphasize the statistical significance of the structures we are analyzing. Applying the same experimental technique and analysis to phantoms of homogeneous samples (e.g., water in a test tube) yields T_1 images that are completely homogeneous at the level of variation apparent in Figures 1 and 2.

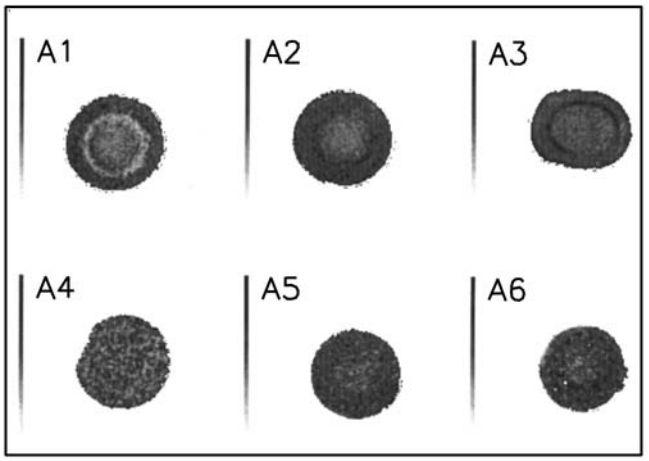

Figure 1. T_1 images of the six catalyst pellets.

The linear grey-scale is different in each panel; it has been chosen to run from the image minimum (white, $T_1 = 0.0$ s) to the image maximum (black) in each case. These are as follows: A1, 0.85 s; A2, 0.74 s; A3, 0.92 s; A4, 1.29 s; A5, 2.00 s; A6, 1.80 s.

Image Analysis

In the following section, the four image analysis techniques applied in this study and their practical implementation are described.

Power-spectrum analysis

The power spectrum is a convenient and powerful way to quantify and analyze the amount of information present on various spatial scales, and is in widespread use (Teuber, 1993). Let us assume that the spatial variation in some quantity Q is given by $f(\boldsymbol{r})$ where $\boldsymbol{r}$ is a position vector—in the present study Q corresponds to the relaxation time T_1, but could in general correspond to any image quantity, for example, spin density. The sampled image is given by $f_{ij} = f(\boldsymbol{r})s(i,j)$, where $s(i,j)$ is the sampling function made up from a sea of delta functions (one at each pixel location), $s(i,j) = \delta(x - i\Delta x)\delta(y-(j\Delta y)$, $i = 1, \ldots, N_x$; $j = 1, \ldots, N_y$. The Fourier transform of the image is another sampled image, $F_{mn} = F(\boldsymbol{k})S(m,n)$, where

$$F(\boldsymbol{k}) = \mathrm{FT}[f(\boldsymbol{r})] = \frac{1}{2\pi}\int_{-Y/2}^{Y/2}\int_{-X/2}^{X/2} f(x,y)e^{ik_x x}e^{ik_y y}\,dx\,dy \qquad (5)$$

and $S(m,n) = \delta(k_x - i\Delta k_x)\delta(k_y - j\Delta k_y)$, $\Delta k_x = 2\pi/N_x\Delta x$; $\Delta k_y = 2\pi/N_y\Delta y$. For simplicity we need consider only the continuous functions $f(\boldsymbol{r})$ and $F(\boldsymbol{k})$, although in practice we must analyze their sampled forms. To investigate spatial correlations (structures) within the image we form the autocorrelation $\phi_a(s,t)$

$$\phi_a(s,t) = \iint f(x,y)f^*(x-s,y-t)\,dx\,dy = f * f^* \qquad (6)$$

where the operator $*$ denotes convolution. The Fourier transform of this autocorrelation function Φ will then be

$$\Phi(\boldsymbol{k}) = |F(\boldsymbol{k})|^2, \qquad (7)$$

and we define the power spectrum $P(k)$ via

$$P(k)dk = \int_0^{2\pi}\Phi(k,\theta)\,d\theta\,dk, \qquad (8)$$

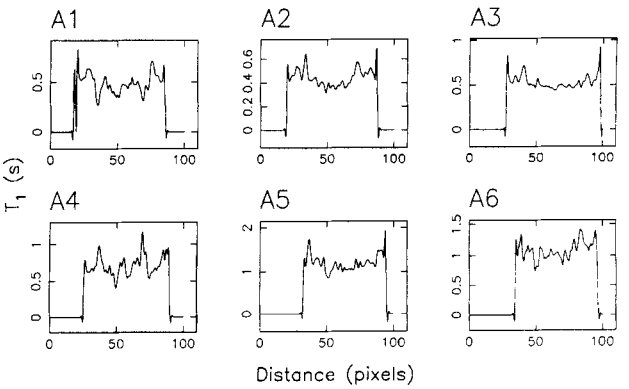

Figure 2. Slices through each of the six images in Figure 1.

The slices were taken through the center of the digitized image. The structure seen in the slices corresponds to the inhomogeneities examined in this article—note the statistical significance of these structures representing deviations of up to 80% of the mean pixel intensity. The errors in T_1 are determined by the accuracy of the fit and in all cases are better than 10%.

where we have transformed to cylindrical polar coordinates ($k_x = k\cos\theta$, $k_y = k\sin\theta$). The power spectrum $P(k)$ therefore measures directly the degree of correlated structure within the image on spatial scales $\approx 2\pi/k$, and in general provides a powerful tool in image recognition and estimation.

Although it is straightforward to calculate the power spectrum of each image shown in Figure 1 from a digital Fourier transform, these data are of extremely limited value in the present context since we are interested in the power spectrum of the pellet inhomogeneities. In particular the experimental power spectra are dominated by the effects of the finite pellet size to such an extent that the less intense correlations arising from the internal structure of the pellet cannot be distinguished. To overcome this problem such that the power spectrum of the inhomogeneities is studied directly the following procedure is adopted. For a given image, f, we can write

$$f(\boldsymbol{r}) = g(\boldsymbol{r}) \cdot b(\boldsymbol{r}), \tag{9}$$

where $g(\boldsymbol{r})$ represents the internal pellet structure and is defined over all space, and $b(\boldsymbol{r})$ is a masking function representing the boundary of the pellet

$$b(\boldsymbol{r}) = \begin{cases} 1 & \text{for pixels within the pellet} \\ 0 & \text{for pixels exterior to the pellet.} \end{cases}$$

Upon Fourier transforming Eq. 9 we obtain $F = G * B$, where $G = \mathrm{FT}(g)$ and $B = \mathrm{FT}(b)$. It is easy to see that B has a significant effect on the power spectrum. If we approximate the pellet geometry to be circular in the image plane, then $B(k) \propto J_0(k)/k$, where $J_0(k)$ is a Bessel function of order 0 and $B(k)$ falls off as $\sim 1/k$ for large k, which means that the effects of the convolution extend over the entire transform plane when the power spectrum is calculated (Eq. 8). To recover $|G|^2$ (the power spectrum of the inhomogeneities) we must deconvolve the effects of B from the power spectrum. This deconvolution is an ill-posed problem, but one that is commonly encountered in other disciplines, especially radio astronomy. In the Appendix we show how the power spectrum of the inhomogeneities can in principle be recovered by application of the iterative deconvolution algorithm CLEAN (Högbom, 1974), although at the expense of considerable data processing.

Of the four image analysis techniques considered here, the traditional power-spectrum analysis is by far the most difficult to implement if proper allowance for the finite size of the pellets in the images is to be made. Of course, in many instances (e.g., microscopy) the sample fills the entire field of view, and in these cases the extension to the basic algorithm we have described is not required—edge effects are still important, but the edges are now those of the finite image that lead to aliasing in the Fourier domain (the treatment of which is well documented, see, e.g., Teuber, 1993).

Cluster analysis

Cluster analysis is a standard image processing/pattern recognition technique used to characterize the nature of the structure present in an image or data set (Teuber, 1993). For our purposes we divide the full range of experimental T_1 values into a finite number of intervals (bins) in T_1 in the same way as a histogram is constructed. Clusters are defined as a set of connected edge-sharing pixels whose T_1 values lie in the same interval in T_1. The output of this analysis is a distribution of cluster sizes for each T_1 bin—a two-dimensional histogram.

The physical motivation for this form of cluster analysis is twofold. First, it quantifies one aspect of visual perception, namely the ability of the brain to pick out ordered (or partially ordered) regions. Second, and indeed more importantly in the current context, it enables us to quantify the degree of inhomogeneity within the structure: Is the structure purely random or are there regions in the image with similar physical properties, such as in our case the relaxation time T_1? One important input parameter is the bin size—in fact, what is important is not the absolute bin size, but rather the number of bins into which the complete range is subdivided. The choice of bin size is to a large extent dictated by the images used: too small a bin size leads to a statistically insignificant number of pixels in each bin, whereas too large a bin size may result in important trends in the data being hidden.

The search for clusters within each T_1 interval is implemented using a list algorithm in which each bin is examined in turn and all pixels in that bin are flagged with flag = 0. The algorithm then proceeds:

1. Increase the count of clusters found.
2. Select one pixel with flag 0 and define a list consisting of this pixel; flag this pixel with the cluster number.
3. For each member of the current list, if their neighbors are pixels with flag 0, add them to a new list of cluster members and flag them with the cluster number.
4. If there are nonzero pixels in the new list, go to step 3 using the new list as input. If there are no new members of the list, but there remain pixels not assigned to any cluster, go to step 1, else stop.

The standard histogram of pixel intensities for a given bin size is simply the projection of this two-dimensional distribution onto the number/pixel-intensity plane (Figure 6). Another useful projection is onto the number/cluster-size plane, which gives the cluster-size histogram (the number of pixels belonging to clusters of a given size, Figure 7). Our images are, of course, slices through a real three-dimensional material—the cluster-size distributions we calculate are indicative of the structure in the *images*, and although there is clearly a close relationship to structures within the material it is important to have this distinction in mind. In this article we have investigated a range of bin sizes between 0.02 and 0.2 in T_1 and find that for this range the main trends between samples persist. We shall therefore only present results in this article for the intermediate case of bin size 0.05, giving a total of 40 bins.

Fractal dimensionality

The images recorded in this study are, for the most part, strongly disordered, although some ordered structures are present, as indicated by the cluster analysis. The fractal concept (Mandelbrot, 1982) provides a method for characterizing strongly disordered systems by treating the disorder as an intrinsic rather than a perturbative phenomenon. We use a fractal analysis here to classify the *shape* of the clusters iden-

tified from the analysis described in the previous section by estimating the fractal dimension of the boundary or perimeter of the clusters. If the clusters were regular and obeyed plane "Euclidean" geometry, then we expect the perimeter C to scale as the "radius" of a cluster, R, as $C \propto R$ and the area A to scale as $A \propto R^2$. For a fractal boundary, the length of the perimeter will depend on the resolution with which the perimeter is measured or alternatively will scale with cluster size R as $C \propto R^D$, where D is the fractal dimension of the boundary (see, e.g., Avnir, 1991, for a brief introduction). The fractal dimension then characterizes the degree of disorder and must satisfy $D_{top} \leq D \leq d$, where D_{top} is the topological dimension of the structure we are analyzing ($D_{top} = 1$ for the boundaries in the image slices considered here) and d is the embedding dimension (i.e., the dimension in which we observe the structure we are analyzing, $d = 2$).

From the images presented here we can only *estimate* the fractal dimension, since a proper analysis would require varying the lengthscale over which measurements are made and examining the limit as this tends to zero (Pfeifer and Obert, 1989), a situation that is not attainable in a real experiment. From the preceding discussion we can obtain a measure of the cluster size from $R \propto A^{1/2}$ and obtain an area-perimeter relationship

$$A \propto C^{2/D}. \tag{10}$$

We use this relation to estimate the fractal dimension from the gradient of the log-area versus log-perimeter plot ($d \log(A)/d \log(C)$) using a form of the boundary extraction method that was employed by Wang et al. (1991) in their analysis of phase-separated structures in polymer blends. Clusters are defined in the same way as the cluster size analysis except that the upper pixel cutoff is set to be greater than any pixel value; clusters are then generated for a range of lower pixel values and their areas and perimeters determined from the number of pixels in a cluster and the number of pixels on the boundary of the cluster, respectively. Plots of cluster area versus cluster perimeter can then be used to obtain the fractal dimension. It is noted that in determining the gradient of the area-perimeter plot we exclude clusters of 10 pixels or smaller, as these structures are too small to use in the fractal analysis (clusters of dimension 3 pixels or less always have the same area-perimeter ratio). An alternative algorithm, "Mosaic Amalgamation" (Russ, 1977), for the calculation of the fractal dimension has been used recently by Davies et al. (1993)—this technique requires the application of an edge-detection filter and then rebinning the image to change the effective resolution; our algorithm is more suitable to the analysis of disorder and heterogeneities where the identification of well-defined structures is not appropriate.

Percolation thresholds

Percolation theory can be applied to the analysis of (randomly) occupied sites in a lattice and is therefore ideally suited to the analysis of image structures where the "lattice sites" are represented by the image pixels. Although the cluster-size analysis we have already discussed can be regarded as part of percolation theory, in this section we concentrate on the percolation threshold. For a given lattice the percolation threshold corresponds to the fraction of sites (chosen at random) that must be occupied for a spanning cluster of sites to exist, where a cluster has the same meaning as discussed earlier, and the spanning cluster is one that forms a continuous cluster across the entire network (Stauffer, 1987). If all sites are equivalent, then for a given (infinite) lattice there exists a unique probability, p_c, the percolation threshold, above which a percolating cluster will form—this threshold is a property of the lattice. We define a spanning cluster as one that joins the external surface of the pellet to the central region of the pellet, where we take the central region to be all those pixels within a circle of radius five pixels at the pellet center. This definition of a spanning cluster is appropriate when considering the effects of transport phenomena within the pellet. For the case appropriate to image analysis all the sites (pixels) are not equivalent since they have associated with them a value for the quantity Q; however, we can still apply percolation ideas in order to examine the "connectivity" of the clusters we have already identified within the image. To do this we shall continue to use the precise definition of a cluster that we have already introduced as a set of connected pixels with values between two defined limits; however, we shall now use percolation analysis to address the question: How ordered (if at all) are the regions of approximate homogeneity of the material property Q (i.e., the clusters) on the scale of the whole pellet? To do this we examine how large we need to make an interval in Q before a spanning cluster is formed. Furthermore, we can do this for any lower limit to the interval Q_l. Two extreme examples will demonstrate that this analysis quantifies larger-scale ordering in an apparently inhomogeneous material. First, if there is no large-scale order, then as the interval in Q (bin size) is increased, pixels join the growing cluster essentially at random and we expect that the percolation threshold as just defined will approach the value for site percolation on a regular square lattice (Stauffer, 1985). If, however, there is large-scale order, for example, a systematic gradient in Q from the outside to the inside of the pellet, we would expect deviations from the pure random result since particular Q values must be included in the prescribed interval before a spanning cluster can form. This behavior will vary systematically with Q_l. The classical definition of the percolation threshold corresponds to $Q_l = 0$.

The detailed method by which the present percolation analysis is performed can be summarized as follows:

1. Select a lower pixel value, Q_l.
2. For each value of Q_l find the lowest value of Q_h such that the pixels with $Q_l \leq Q \leq Q_h$ form one or more spanning clusters. The value of Q_h is calculated to the required precision (2% in this case) using a binary chop algorithm.
3. Define the percolation threshold as the fraction of pixels with pixel values in the range $Q_l \leq Q \leq Q_h$.
4. Repeat steps 1, 2, and 3 for a range of Q_l.

For each image we generate a plot of percolation threshold, p_c, as a function of lower pixel value Q_l; a percolating cluster does not exist above some value of Q_l.

Results

In this section we apply the four methods of image analysis described in the previous section to each of the six pellet

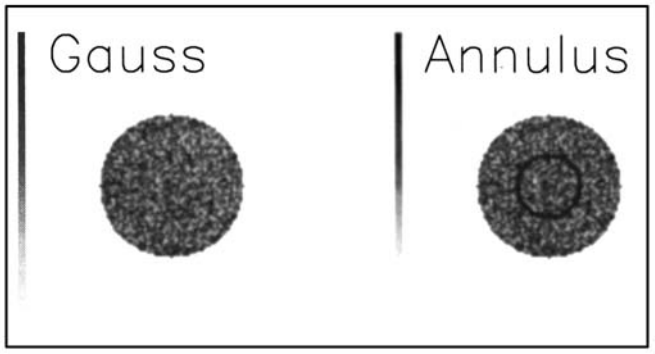

Figure 3. Simulated T_1 images, Gauss and Annulus.

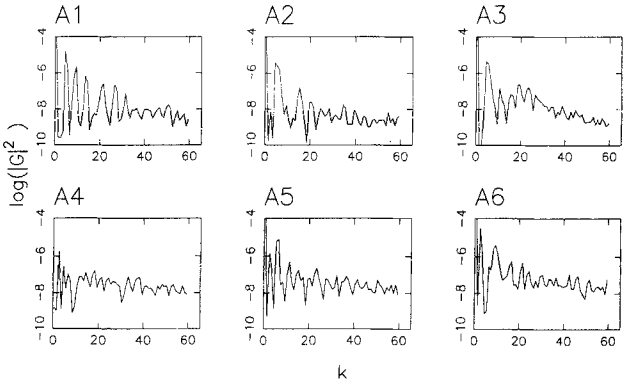

Figure 4. Power spectra for the six catalyst pellet images in Figure 1.

images and also to two simulated pellet images. The simulated pellet images are used for comparison purposes so that structural information present in the images of the catalyst pellets can be identified. Construction of the simulated pellet images was achieved as follows. The distribution of pixel intensity values for the catalyst pellets was approximated by a Gaussian distribution of approximately the same variance as the experimental distribution; images were then constructed by assigning values from this distribution at random to pixels within a region of the image of the same size and shape as the actual pellet images. In addition to these "randomly" populated images we constructed further simulated images by introducing regular features such as disclike and annular structures. We shall refer in detail to two such simulated images in our discussion of the analysis procedures. These images represent two extremes, the purely randomly populated image (Gauss) and an image with an annular feature (Annulus) similar in appearance to the structures seen in pellets A1, A2, and A3. These two images are shown in Figure 3.

The images of the six catalyst pellets are influenced by both the presence of noise and by convolution with an unknown function characterizing the NMR spectrometer and the image acquisition process. Detailed interpretation of images and the structures they contain must take proper account of these experimental limitations. All experimental images presented here were obtained under identical acquisition conditions and therefore interpretation of similarities and differences between the images is greatly simplified.

Power-spectrum analysis

In Figure 4 we compare the power spectra of the inhomogeneities, $|G|^2$, for the six pellets under consideration here. The factors to note in the spectra are the overall envelope (related to the size of large-scale coherent structures in the images) and the relative amount of "power" at low and high spatial frequency. These attributes enable the structure apparent in the images themselves to be quantified by determining the most important spatial scales and their degree of coherence within the image. The power spectra for samples A4, A5, and A6 are similar, all showing relatively little low-frequency power consistent with the lack of large-scale structure in the T_1 images. In contrast, the spectra for A1 and A3 show some low-spatial-frequency structure in the range $k =$ 10–40 pixels (in the Fourier domain) corresponding to spatial scales between ~ 6 and ~ 25 pixels in the T_1 images. The structure at high spatial frequencies is well above the noise level but shows no similarity between the samples. The lack of definite spectral features in any of the pellets especially at high spatial frequencies indicates that there is no preferred spatial scale or periodicity, a result supported by the cluster analysis discussed later. Finally, we note that from these power spectra we can identify A4 as the sample showing the least coherent structure—a result that is consistent with the visual appearance of the T_1 images. Although we have isolated the power spectra of the inhomogeneities, their interpretation is not straightforward, and other methods are required to quantify the nature of the inhomogeneities observed in these images.

Cluster analysis

In Figures 5, 6, and 7 we show the results of the cluster-size analysis for the six catalyst pellets and the two simulated pellet images. In Figure 5 we show the cluster distribution functions as isometric surfaces, while in Figures 6 and 7 we show the pixel-value histograms (T_1 histograms) and the cluster-size histograms, respectively. The relationship between T_1 and the surface area to volume ratio characteristic of the pore space discussed earlier suggests that the T_1 histograms provide a representation of the diffusionally averaged mean pore-size distribution for each sample— at least in principle, a corollary of this relationship is that the two-dimensional cluster-size distributions allow the pore-size distributions for specific clusters to be determined.

An immediate observation is that the shape and width of the population/T_1 histograms differ markedly between images A1 and A6. The same observation is made for the population/cluster-size histograms. In this set of images the width of the T_1 distribution correlates inversely with the width of the cluster-size distribution. The implication of this result is that a pellet characterized by a narrow T_1 (pore-size) distribution is associated with a macroscopically heterogeneous voidage, that is, different macroscopic spatial regions within the pellet are associated with pores of significantly different size. In contrast, a pellet with a wide T_1 distribution tends to be associated with a macroscopically homogeneous pore network in which pores of a range of diameters are distributed

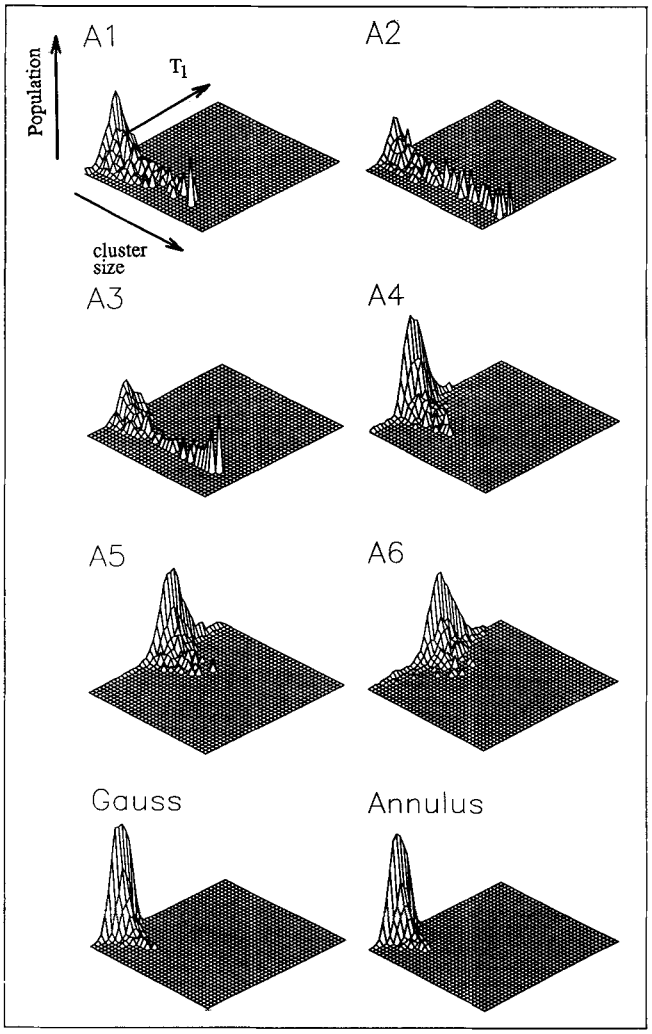

Figure 5. Cluster-size distributions for the six catalyst pellet images and two simulated images.

Pixel intensity values increase along the x-axis and cluster size increases down the y-axis. The surface is scaled to the number of pixels involved in clusters of a given size for a given bin in intensity. The bin size in intensity shown here is 0.05. For three pellets, A1, A2, and A3, the distributions have been truncated at a cluster size of 35. Beyond this size clusters exist for these pellets as follows: A1 has one cluster of size 102 pixels for $0.4 \le T_1 \le 0.45$ and one of size 340 pixels for $0.45 \le T_1 \le 0.5$; A2 has a total of six clusters of size ~ 100 for $0.4 \le T_1 \le 0.5$ and two large clusters of size 233 and 317 pixels for $0.45 \le T_1 \le 0.5$ and $0.35 \le T_1 \le 0.4$, respectively; A3 has two clusters of size ~ 100 for $0.5 \le T_1 \le 0.6$, two of size ~ 200 in the same range, and one cluster of size 594 pixels for $0.45 \le T_1 \le 0.5$; Annulus has one cluster of size 365 for $0.4 \le T_1 \le 0.5$.

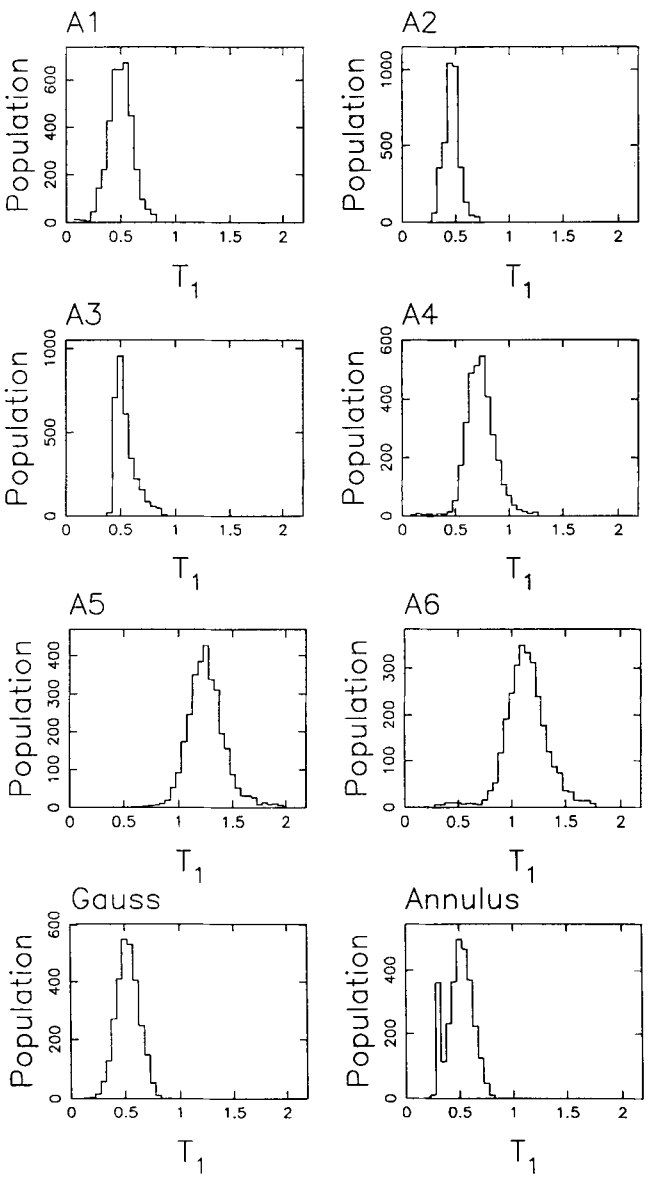

Figure 6. Pixel intensity (T_1) distributions derived from the 2-D cluster distributions in Figure 5.

The bin size is 0.05.

homogeneously throughout the pellet. Further insight into the structure of the porous pellets is obtained by considering the cluster analysis applied to the two simulated pellet images. For both the Gauss and Annulus images the width of the distribution of pixel values decreases as a function of increasing cluster size—for the Annulus image there is one large cluster represented, but the cluster-size distribution shows a discontinuity between the main part of the distribution and the single large cluster. This behavior is consistent with that expected from simple statistical considerations (the larger clusters will involve the pixels with the most common value, i.e., those close to the mean for a symmetric distribution). For pellets A4, A5, and A6, the shapes of the distributions (see Figure 5) and the falloff in the cluster-size histograms (Figure 7) are not significantly different from the random case represented by the simulated Gauss image; however, the fractal and percolation analyses to be discussed later will both reveal that there is topological structure in the images not apparent directly from the cluster analysis. The images of pellets A2 and A3 appear to show coherent structures, and this is confirmed by the cluster-size analysis. Both images contain a few very large clusters (Figure 5). The cluster analysis also reveals additional structure in pellets A2 and A3; their cluster-size distributions do not fall off quickly with increasing cluster-size, but rather show a continuous distribu-

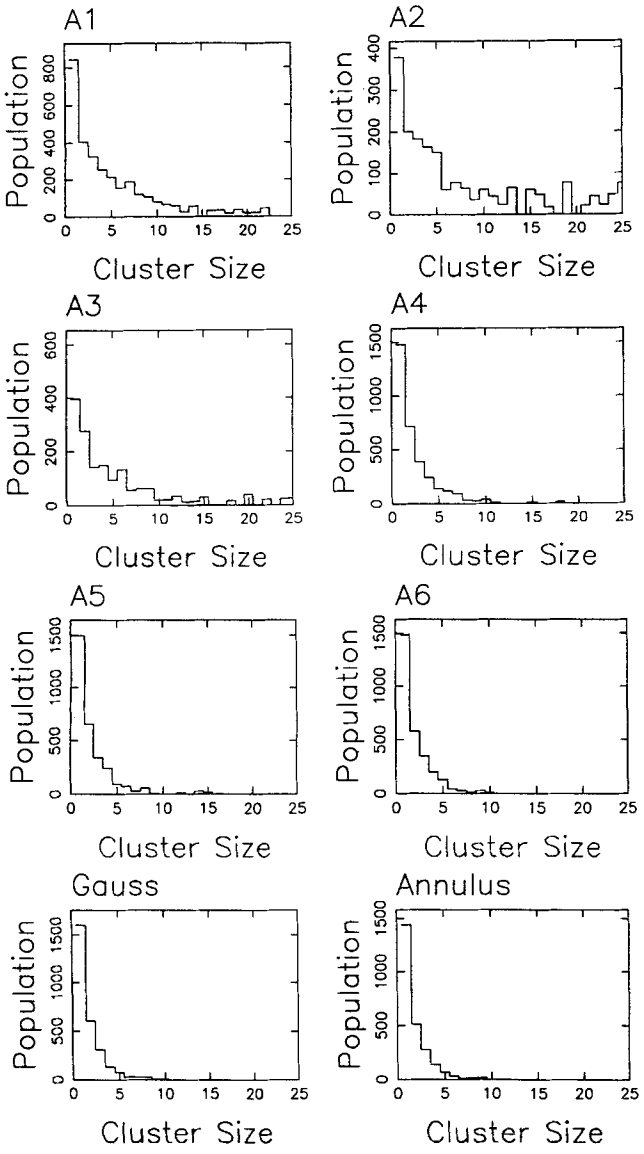

Figure 7. Cluster size distributions derived from the 2-D cluster distributions in Figure 5.

The bin size is 0.05. The distributions have been truncated to emphasize the low-cluster-size structure (see Figure 5 for more details).

tion of cluster sizes out to cluster sizes of order 100 pixels (Figure 7 and see also Figure 5). This long tail in the cluster-size distribution distinguishes the real pellets from the simulated pellet image Annulus. Whereas Annulus has a visual appearance similar to the real pellet images, in the latter the annular ring is just the most noticeable feature of a complete hierarchy of structures (clusters) up to and beyond the scale-size of the ring, but confined within a narrow range of T_1. Both A2 and A3 also contain clusters that are larger than the cluster size necessary to produce the ringlike feature in the images; this additional structure may arise from a uniform region interior to the observed ring. Despite the similarity in appearance between images A1, A2, and A3 in terms of an apparent ringlike structure, the cluster analysis reveals considerably less structure in pellet A1 than in either pellet A2

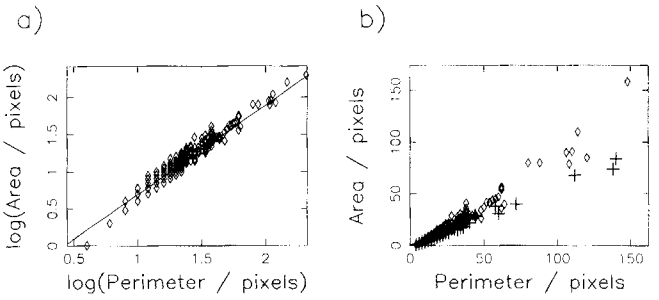

Figure 8. Fractal analysis.

Area-perimeter data (◇) for homogeneous clusters within the six pellet images are shown on (a) log-log, and (b) linear axes. In (b) the area-perimeter data for the two simulated images are also shown (+). The plot of the data using linear axes demonstrates clearly the differing characteristics of the real and simulated images.

or pellet A3 (Figure 7). These differences, which are very marked in the cluster-size analysis, are not immediately apparent in the power-spectra analysis (Figure 4).

Fractal dimensionality

In Figure 8 we show an area-perimeter plot using a bin size of 0.05 (for comparison with the results presented for the cluster analysis) for all six catalyst pellet images together with the two simulated data sets, Gauss and Annulus. In Figure 8a we show the data for the six catalyst pellets only on a log-log plot to emphasize that the images for all experimental samples follow the same trend; in Figure 8b we show the data for all eight images displayed using linear axes. It is clear that the results for all six pellets agree well and give a slope in the log-area vs. log-perimeter plot of 1.26 ± 0.02 corresponding to a fractal dimension of 1.58 ± 0.03 determined using all of the data. It is apparent that the two simulated pellet images, having similar cluster-size properties, have very different fractal dimensionalities, and therefore the fractal dimension provides us with complementary information describing the structure of the inhomogeneities within the image. This result is insensitive to the range of lower pixel values used, and we have investigated step sizes between 0.02 and 0.2 (for the cluster-size analysis) (see Table 1). It is clear from Table 1 that the results obtained for each pellet for a given bin size agree to within our estimated error of 0.03 except at the extreme when the bin size is 0.2. For this interval in T_1 the clusters become large compared to the image size itself (the pellet image only occupies the central region of a 128×128 grid), hence the estimate of fractal dimension becomes unreliable and we therefore base our quoted values on smaller bin sizes when the analysis is less affected by the finite image size.

It is useful to consider the behavior we would expect for the fractal dimension D. Clearly, for large regular structures (clusters) we expect D to approach the topological dimension of unity, which is appropriate for the cluster perimeter that is simply a line. Such a structure might be expected if the regions of heterogeneity resulted from, say, the fabrication of the pellet involving pelleting of smaller particles. For small clusters we must take account of the quantized nature of the image; for clusters containing only a few (≤ 8) pixels the

Table 1. Fractal Analysis

	Fractal Dimension, D Bin Size			
Sample	0.02	0.05	0.1	0.2
A1	1.56	1.56	1.56	1.58
A2	1.62	1.61	1.63	1.68
A3	1.56	1.54	1.54	1.61
A4	1.64	1.64	1.63	1.73
A5	1.56	1.56	1.53	1.61
A6	1.59	1.59	1.64	1.69
All data	1.58	1.58	1.59	1.64
Gauss	1.75	1.75	1.75	1.77
Annulus	1.72	1.72	1.73	1.76

fractal dimension will approach 2 in all cases since any cluster of this size cannot contain any *internal* pixels (i.e., pixels that do not count toward both the area and the perimeter), and both the area and perimeter will increase approximately linearly with the number of pixels in the cluster. This effect is apparent in our data, and we have therefore not included data points associated with clusters of less than 10 pixels in determining the fractal dimensions. A high fractal dimension is also expected when the structures are filamentary, or of the form normally associated with diffusion-limited aggregation (Meakin, 1989). Our results show that despite marked differences between the pellet images in terms of their cluster-size distributions they share a universal fractal dimensionality suggesting that the *shape* of the clusters, or regions of heterogeneity, is intrinsic to the material/fabrication process associated with the pellet. In this case, it is also interesting that the fractal dimension for the images of the real pellets is less than that for the simulated images, proving that there is in fact more order to the distribution of irregularities than the random distribution associated with the simulated data. Finally, we note that including even a very well-defined feature (in the Annulus simulated pellet) does not alter significantly the fractal dimensionality, and therefore the fractal analysis presented here is seen to be a technique that is a sensitive probe of the underlying structure of inhomogeneities within an image.

Percolation threshold

in Figure 9 we show plots of the percolation threshold, p_c, as a function of $X = Q_l/\overline{Q}$, where $\overline{Q}$ is the mean value of pixels within the region of the image defined by the pellet. It is useful to first consider the percolation characteristics of the two simulated pellet images. For the Gauss image we see that at low X, $p_c \approx 0.57$, which is close to the theoretical value of 0.59 for site percolation on a square lattice (Stauffer, 1985). This result is to be expected since for the Gauss image the pixel values have been assigned at random from the prescribed distribution—we therefore do not expect that the topology of the lattice corresponding to the image would differ significantly from that of a regular square lattice with equivalent sites. The difference between p_c for the square lattice and Gauss may be due to the small size of our lattice —a theoretical percolation threshold is defined for an infinite lattice (we do not expect the shape of the lattice boundary, in this case nearly circular, to be significant). Above Q_l

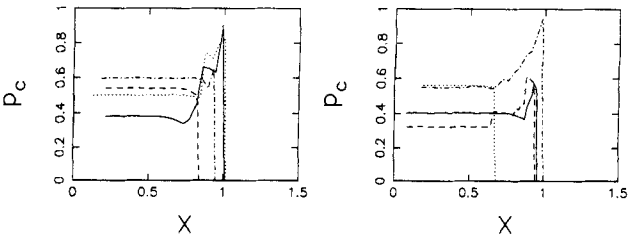

Figure 9. Percolation threshold, p_c, as a function of dimensionless pixel value X.

(a) A1 ——, A2 – – –, A3 ·—·—, A4 ····; (b) A5 ——, A6 – – –, Gauss ·—·—, Annulus ····.

$= \overline{Q}$ $(X = 1)$ a percolating path can no longer be found and close to this limiting value of X, p_c rises significantly. Again this behavior is to be expected since above some pixel level we will have excluded sufficient pixels that a percolating path cannot exist, and close to this limit we must include essentially all available pixels in the percolating path. For the simulated image containing a coherent structure (Annulus) the behavior is very different. At low X, p_c again has a value close to the theoretical value for the square lattice, but now the limiting value of X beyond which a percolating path cannot be found occurs for $X \ll 1$; clearly the coherent structure *must* be included in the pixels assigned to the percolating path, and this provides a sharp cutoff at a value of X appropriate for the coherent structure.

We shall now consider the results for the real pellet data in the light of our discussion of the simulated images. In all cases the p_c for low X is either comparable with the theoretical value of 0.59 or less. For the three pellets A1, A5, and A6 their value of p_c for $X \ll 1$ is much lower than 0.59, suggesting that there is structure in the images that is not apparent from a visual inspection but that leads to a topological structure that reduces the percolation threshold (i.e., it is easier to find a percolating path) compared to that characterizing the random distribution. This must be an intrinsic difference related to the underlying structure of the pellets in the same way as the fractal dimension discussed earlier shows a systematic difference between the experimental and simulated pellet images. Despite these lower values for p_c, all three pellets show cutoffs in the percolation thresholds close to $X = 1$, and we take this as a clear indication of a lack of coherent structures in these pellets, despite some visual indications to the contrary for pellet A1. The results for pellet A4 are most closely related to the results for the random structure, and we recall that the power-spectrum analysis indicated that this pellet showed the least structure. Pellet A2 shows some evidence for coherent structures with a cutoff in its percolation curve at values of $X < 1$—there is also some slight indication of coherent structure in pellet A3. Again this behavior is reflected in some of the other results, especially the cluster-size distributions that show extended distributions for both pellets A2 and A3 and also to a lesser extent in the power spectra. In this study percolation analysis is seen to be a very sensitive tool in the analysis of structures and their interconnection.

Discussion

The four techniques we have considered clearly provide us

with complementary information. The power spectra reveal information on spatial correlations over a range of length scales, although no specific structural feature characterizing the pellets studied here could be identified. In this particular study, the cluster-size analysis provides more useful information in terms of characterizing the scale size of inhomogeneities within the image. It is noted that if the images under study had exhibited periodic structures, such as low spatial-frequency ripples, the power-spectrum analysis would have been the only method of the four to reveal directly this structural property.

The cluster-size analysis provides a wealth of information, and we have not discussed here all the ways in which this information could be used—some possibilities include calculating statistics such as cluster moments to characterize the shape of a given cluster. The cluster-size histogram provides information on the scale size of structures present in the image and, periodic structures aside, provides very much the same information as that available from the power spectra. Both the cluster-size histogram and the overall structure in the cluster-size/pixel-intensity plane provide a good way of quantifying the amount of regular "coherent" structure present in an image. Much of the information present in the cluster-size analysis is not immediately apparent from visual inspection; it is only when the experimental cluster distributions are compared with those of model or simulated images that structural characteristics can be identified. For example, the simulated image Annulus does not reproduce the cluster distributions for the images with visual ringlike structures; the real images contain structures on all scales up to and beyond the scale represented by the ring in the image.

The shape of the clusters can be analyzed in a number of ways—we have mentioned moment analysis as one method —but the determination of the fractal dimension of the images of the six pellets has been particularly revealing. Both visually and in the majority of the image analysis procedures we have applied to the pellet images, significant variation in properties has been found. However, the fractal dimensions of all the pellets are, to within the errors of the analysis, identical, suggesting that the underlying structure of the pellet is determining the fractal dimensionality. The percolation threshold also provides information on the interconnectivity of the regions of differing homogeneity identified using the cluster analysis. Again interpretation of the behavior of the percolation threshold is greatly aided by comparison of the experimental results with simulated model images.

The aim of this study has been to identify and apply image analysis techniques to characterize structural inhomogeneities within images of porous catalyst support pellets. Each of the four image-analysis techniques considered here provides complementary information, and the interpretation of that information taken as a whole is aided by constructing simulated model images with known structures. It is evident that while the simulated images in many ways provide a good model for the experimental images, they fail to model simultaneously the results from *all* the analysis techniques considered. Traditionally, a one-dimensional pore-size distribution, determined by mercury porosimetry or nitrogen adsorption, would be used to constrain any structural model describing a porous solid. While the truly microscopic properties of the material are described using such techniques, the micron-scale structural variations within the medium are ignored. The results reported here suggest that it is now possible to develop structural models of porous media that can be more fully validated against experimental measurements performed on real materials. Realistic models of the catalyst support pellets studied here should be characterized by the same fractal dimension as that determined experimentally. Properties of a specific pellet might require additional correspondence between model and experiment of power spectrum, cluster analysis, and percolation threshold.

Conclusion

Transport within a given porous medium is determined by the structure of that medium. While nitrogen adsorption and mercury porosimetry analysis produce a one-dimensional pore-size distribution characterizing a porous solid, experimental techniques have not yet been used to determine the spatial variation in pore size and the clustering behavior of regions of similar voidage (or pore size) within such materials. In this article, spin-lattice relaxation time images of six porous catalyst support pellets drawn from a single batch are reported. These images show significant spatial variation in intensity, suggesting macroscopic variations of locally averaged mean pore size within the sample. Four image analysis techniques were applied to the data. Most interestingly, the fractal dimension of all six images was the same, suggesting that this characteristic should be reflected in any structural model constructed to predict, for example, transport properties associated with this batch of catalyst support pellets. Further characteristics, particular to each individual pellet within the batch, can also be obtained: power-spectra and cluster-size analyses characterize structural correlations on varying length scales and the clustering of regions of similar property (in this case T_1), respectively, while percolation analysis quantifies the connectedness of homogeneous clusters within the image.

Acknowledgments

L. F. Gladden gratefully acknowledges the Process Engineering Committee of the SERC for the award of an NMR spectrometer, and ICI for the award of an ICI Fellowship. M. P. Hollewand thanks the Oppenheimer Trust and Trinity College, Cambridge, for financial support. We also thank the referees for helpful comments on the manuscript.

Notation

B = Fourier transform of b
B_0 = static magnetic field strength
C = perimeter
D = fractal dimensionality
$\mathfrak{D}$ = bulk diffusion coefficient
F = Fourier transform of image data
G = Fourier transform of g
G = magnetic field gradient
M = magnetization
N = image dimension
P = power spectrum
Q = image quantity
R = cluster radius
S = sampling function in Fourier space
S = NMR signal intensity
T_1 = NMR spin-lattice relaxation time
V = volume

VD = variable delay time
X = dimensionless image quantity
b = function representing pellet boundary
d = embedding dimension
f = image intensity distribution
g = function representing inhomogeneities
k = radius in Fourier space
i, j = pixel labels
$\boldsymbol{k}$ = Fourier-space vector
p_c = percolation threshold
r = pore radius
$\boldsymbol{r}$ = position vector
s = sampling distribution (real space)
t = time
s, t = dummy coordinates
x, y = spatial coordinates

Greek letters

Φ = image spatial power
α = constant
γ = gyromagnetic ratio
β = constant
τ = mean lifetime
λ = thickness of surface layer
ϕ_a = autocorrelation function
ρ_s = spin density
ρ = interfacial spin-relaxation constant
ω = precession frequency
θ = angle in Fourier plane

Subscripts

0 = initial value
i, j = pixel labels
l = lower limit
top = topological
x, y = spatial coordinates
B = bulk
S = surface

Literature Cited

Avnir, D., "Fractal Geometry—A New Approach to Heterogeneous Catalysis," *Chem. Ind.*, **24**, 912 (1991).

Brownstein, K. R., and C. E. Tarr, "Spin-Lattice Relaxation in a System Governed by Diffusion," *J. Magn. Reson.*, **26**, 17 (1977).

Burganos, V. N., and A. C. Payatakes, A. C., "Knudsen Diffusion in Random and Correlated Networks of Constricted Pores," *Chem. Eng. Sci.*, **47**, 1383 (1992).

Callaghan, P. T., *Principles of Nuclear Magnetic Resonance Microscopy*, Clarendon, Oxford (1991).

Davies, E. S., T. A. Carpenter, L. D. Hall, and C. Hall, "NMR Imaging of Fractal Fingering in Hele-Shaw Cells," *AIChE J.*, **39**, 510 (1993).

Fukushima, E., and S. B. W. Roeder, *Experimental Pulse NMR: A Nuts and Bolts Approach*, Addison-Wesley, Reading, MA (1981).

Högbom, J., "Aperture Synthesis with a Non-Regular Distribution of Interferometer Baselines," *Astrophys. J. Suppl.*, **15**, 417 (1974).

Hollewand, M. P., and L. F. Gladden, "Bond Percolation and Conduction in Random and Regular Networks: Topological Effects at Low Coordination Numbers," *J. Phys.: Condens. Matter*, **4**, 5757 (1992a).

Hollewand, M. P., and L. F. Gladden, "Modelling of Diffusion and Reaction in Porous Catalysts Using a Random Three-Dimensional Network Model," *Chem. Eng. Sci.*, **47**, 1761 (1992b).

Hollewand, M. P., and L. F. Gladden, "Representation of Porous Catalysts Using Random Pore Networks," *Chem. Eng. Sci.*, **47**, 2757 (1992c).

Hollewand, M. P., and L. F. Gladden, "Heterogeneities in Structure and Diffusion within Porous Catalyst Support Pellets Observed by NMR Imaging," *J. Catal.*, **144**, 254 (1993).

Kirkpatrick, S., "Percolation and Conduction," *Rev. Mod. Phys.*, **45**, 574 (1973).

Lowell, S., and J. E. Shields, *Powder Surface Area and Porosity*, 2nd ed., Chapman & Hall, London (1984).

Mandelbrot, B. B., *The Fractal Geometry of Nature*, Freeman, San Francisco (1982).

Meakin, P., *Fractal Geometry—A New Approach to Heterogeneous Chemistry*, D. Avnir, ed., Wiley, New York, p. 131 (1989).

Mendelson, K. S., "Magnetic-Relaxation in Porous-Media," *Magn. Reson. Imaging*, **9**, 651 (1991).

Munn, K., and Smith, D. M., "A NMR Technique for the Analysis of Pore Structure—Numerical Inversion of Relaxation Measurements," *J. Colloid Interf. Sci.*, **119**, 117 (1987).

Oger, L., C. Gauthier, C. Leroy, J. P. Hulin, and E. Guyon, "Heterogeneities and Characteristic Lengths in Porous Media," *Int. Chem. Eng.*, **32**, 674 (1992).

Pfeifer, P., and M. Olbert, *Fractal Geometry—A New Approach to Heterogeneous Chemistry*, D. Avnir, ed., Wiley, New York, 11 (1989).

Reyes, S. C., and E. Iglesia, "Effective Diffusivities in Catalyst Pellets: New Model Porous Structures and Transport Simulation Techniques," *J. Catal.*, **129**, 457 (1991).

Russ, J. C., "Feature-specific Measurement of Surface Roughness in SEM Images," *Part. Charact.*, **4**, 22 (1977).

Sahimi, M., "Diffusion-Controlled Reactions in Disordered Porous Media—I. Uniform Distribution of Reactants," *Chem. Eng. Sci.*, **43**, 2981 (1988).

Sahimi, M., G. R. Gavalas, and T. T. Tstotis, "Statistical and Continuum Models of Fluid-Solid Reactions in Porous Media," *Chem. Eng. Sci.*, **145**, 1443 (1990).

Sotirchos, S. V., and V. N. Burganos, "Analysis of Multicomponent Diffusion in Pore Networks," *AIChE J.*, **34**, 1106 (1988).

Stauffer, D., *Introduction to Percolation Theory*, Taylor & Francis, London (1985).

Teuber, J., *Digital Image Processing*, Prentice-Hall, Hemel Hempstead, p. 147 (1993).

Wang, Z.-Y., M. Konno, and S. Saito, "Application of Digital Image-Analysis to the Characterization of Phase-Separated Structures in Polymer Blend," *J. Chem. Eng. Japan*, **24**, 256 (1991).

Wilkinson, D. J., D. L. Linton, and L. M. Schwartz, "Nuclear Magnetic Relaxation in Porous Media: The Role of the Mean Lifetime $\tau(\rho, \mathfrak{D})$," *Phys. Rev. B.*, **44**, 4960 (1991).

Woessner, D. E., "Spin Relaxation Processes in a Two-Proton System Undergoing Anisotropic Reorientation," *J. Chem. Phys.*, **36**, 1 (1962).

Appendix

In this Appendix we consider the details of the method employed to obtain the power spectra of the inhomogeneities, making proper allowance for the finite extent of the pellets in each image. As explained in the main text, the problem is one of deconvolution of the function B from the Fourier transform of the experimental data F to obtain the power spectrum of irregularities G^2. This situation is similar to the deconvolution problem encountered in radio astronomy where the effects of the sampling of the Fourier plane (resulting from measurements with a finite number of interferometer spacings) results in a convolution in the image plane. There are many techniques to perform this deconvolution, which as here is an underdetermined problem, but one particularly simple algorithm to implement is the CLEAN method (Högbom, 1974). The CLEAN algorithm is iterative. At each iteration the absolute maximum on the image to be deconvolved (F) is located, and the function to be deconvolved (B) is shifted and centered at this maximum in F. Function B is then scaled to a fraction of this maximum intensity (usually between 5% and 20%), and the scaled, shifted function B is subtracted from F to produce a "residual" image F'; the fraction subtracted and the location of the maximum to which B was scaled are assigned to a new image, the CLEAN image. The process continues by finding the abso-

lute maximum on the residual image F', generating another entry in the CLEAN image and updating the residual image. The iterative cycle is halted when the absolute maximum on the residual image is below a user-defined level. Finally, the residual image (assumed now to be essentially noise) is added to the CLEAN image after the latter is convolved with a Gaussian of the same width as the central region of B (to avoid problems associated with superresolution).

In order to apply this algorithm to the problem of deconvolving the power spectrum, two steps were required:

1. Construct the function b representing the region of the pellet image—this was simply achieved using a gate level on the image and assigning every pixel with a value below the gate to the region external to the pellet and all other pixels to the internal region of the pellet.

2. The CLEAN algorithm operates on real images; however, the Fourier transform of the pellet images results in a complex image. To overcome this problem an image of twice the size of the original was generated. With the original image in the upper-left quadrant, the lower-left quadrant was then formed so that the image was "even" about its center. By this construction the Fourier transform of this symmetrized image was real (no information is lost by this process, as the transform plane is now twice as large). This symmetrizaton procedure was applied to both the experimental images and the corresponding boundary masks, and the "real" transforms of the symmetrized image were CLEANed.

This symmetrization was performed for each pellet image, followed by a CLEAN to a level below the noise level on the transform (taking more than 8000 iterations of the CLEAN algorithm). The power spectra of the inhomogeneities were then recovered from these deconvolved Fourier-plane data by taking the inverse transform, extracting the image in the upper-left quadrant only, then performing a forward transform on this image (which effectively has had the edge of the pellet removed), and finally integrating numerically to produce the power spectra. These final steps were required to recover an approximately circularly symmetric transform appropriate to the pellet shapes in the images.

Manuscript received Oct. 12, 1993, and revision received Apr. 15, 1994.